Imaging voids and defects inside Li-ion cathode $LiNi_{0.6}Mn_{0.2}Co_{0.2}O_2$ single crystals

Isaac Martens,[†] Victor Vanpeene,[†,‡] Nikita Vostrov,[†] Steven Leake,[†] Edoardo Zatterin,[†] Jeremie Auvergniot,[¶] Jakub Drnec,[†] Marie-Ingrid Richard,[†,§] Julie Villanova,*,[†] and Tobias Schulli*,[†]

†ESRF - The European Synchrotron, 71 Avenue des Martyrs, Grenoble 38000, France
‡Université Grenoble Alpes, CEA Grenoble, LITEN, 17 rue des Martyrs, 38054 Grenoble, France
¶Umicore, France
§Univ. Grenoble Alpes, CEA Grenoble, IRIG, MEM, NRX, 17 rue des Martyrs 38000 Grenoble, France

E-mail: julie.villanova@esrf.fr; schulli@esrf.fr

Abstract

Li-ion battery cathode active materials obtained from different sources or preparation methods often exhibit broadly divergent performance and stability, despite no obvious differences in morphology, purity, and crystallinity. We show how state-of-the-art, commercial, nominally single crystalline $LiNi_{0.6}Mn_{0.2}Co_{0.2}O_2$ (NMC-622) particles possess extensive internal nanostructure even in the pristine state. Scanning X-ray diffraction microscopy reveals the presence of interlayer strain gradients and crystal bending attributed to oxygen vacancies. Phase contrast X-ray nano-tomography detects substantial quantities of nano-voids hidden inside the bulk.

Abbreviations

SXDM, NMC, nano-CT

Keywords

Li-ion batteries, SXDM, NMC, NCM, nano-tomography

Introduction

The ongoing decarbonization of electricity grids is limited by the cost and capacity of energy storage.[1] Batteries with higher energy density and operational lifetimes are needed for applications ranging from grid storage to automotive transport. One strategy to improve the stability of Li-ion batteries is to fashion the cathode active material from micron-sized single crystals instead of polycrystalline aggregates.[2] Single crystal layered materials such as $LiNi_{0.6}Mn_{0.2}Co_{0.2}O_2$ (NMC-622) have demonstrated unprecedented cycling life in laboratory environments, theoretically enabling batteries which could operate for many decades.[3,4] This is due to the lack of defects and grain boundaries which concentrate stress.[5] Cracks nucleate and propagate from these features, leading to pulverization, lowered capacity, and an increase of internal resistance over time.[6,7] Intracrystal heterogeneities and fracturing therefore limit the maximum useful cycling rate, the maximum cell voltage, and the stability of the surface.[4,6,8–10]

Manufacturing high-performance active materials at scale with controlled crystal quality is challenging. The fabrication of single crys-

tal cathode materials typically involves several complex processing steps which must be optimized, including synthesis, annealing, grinding, and coating application.[2] Most of the single crystal materials reported in the academic literature are fabricated at small scale (often without mentioning suppliers) with no straightforward or validated methods to evaluate the quality of the product.[11] For new materials whose durability is measured in decades, it is completely impractical to validate aging through long-term cycling prior to commercial release, and heuristic approaches must therefore be developed which can predict future performance.

This quality assurance problem co-exists with issues where different groups evaluating materials with nominally identical crystal structures obtained from different sources or different synthetic routes obtain widely varying cell performance and stability.[2,5,12] The observed performance variation can be attributed to defects, porosity, surface impurities, coating homogeneity, crystallographic site occupancies, and other microstructural properties. While the academic literature refers to this class of active materials as a "single crystal" morphology, industry partners and the patent literature often prefer the term "monolithic" instead, which better acknowledges the internal structural diversity of the particles.[13]

Unfortunately, there are few tools suitable for determining the crystal microstructure of these cathode particles. The peak widths are generally much too sharp for lineshape analysis by conventional powder X-ray diffraction,[11] but the micron-sized particles are still too small for even modern laboratory single crystal diffraction ($\leq 30\,\mu m$). Scanning electron microscopy is commonly employed, but provides very little information about internal microstructure unless combined with serial focused ion beam (FIB) milling. Transmission electron microscopy yields high spatial resolution, but has the same drawback of using laborious ion milling to prepare ultrathin sections.[8] Advanced characterization tools are urgently required to scale-up manufacturing of these materials, and guide development of new cathode chemistries.[14] A variety of powerful synchrotron techniques are being optimized for these applications, towards higher throughput, quality, and ease of data analysis.[7,15–17]

In this work, we show how nano-focused Scanning X-ray Diffraction Microscopy (SXDM) and X-ray nano computed tomography (nano-CT) reveal different aspects of the microstructure hidden inside single crystal cathode particles. We demonstrate an example of state-of-the-art commercial $LiNi_{0.6}Mn_{0.2}Co_{0.2}O_2$ (NMC-622) which exhibits large internal heterogeneities that are nearly impossible to observe using conventional techniques. SXDM probes the variations in crystallographic ordering at the nanoscale, while nano-CT exposes voids, porosity, and microcracks throughout the crystals. Structural descriptors which allow universal, quantitative ranking of crystal quality are developed, and the inter- and intra-particle heterogeneities of the sample are explored.

Results and discussion

Strain imaging

SXDM was used to map the interlayer d-spacing of NMC-622 particles *ex situ*. Details regarding the microscope and data analysis have been published elsewhere.[18,19] Briefly, a nanofocused X-ray beam is rastered across the sample of isolated particles dispersed on a substrate. The diffraction signal from the 003 NMC reflection at each pixel is measured with high angular resolution. A rocking curve is performed, collecting a stack of images while rotating the aligned microcrystal through the Bragg reflection. The 2D real-space images plus the 3D reciprocal space maps for each pixel produce a 5 dimensional dataset. The peak position of the diffraction is fitted for each pixel, from which crystallographic structural parameters can be extracted (Fig. S1).

Figure 1 shows the SXDM results from imaging a single NMC particle. While any reflection can be measured, the 003 peak was selected because it corresponds to the spacing between layers of the transition metal slabs (Fig. 1A), and is therefore quite sensitive to heterogeneities in
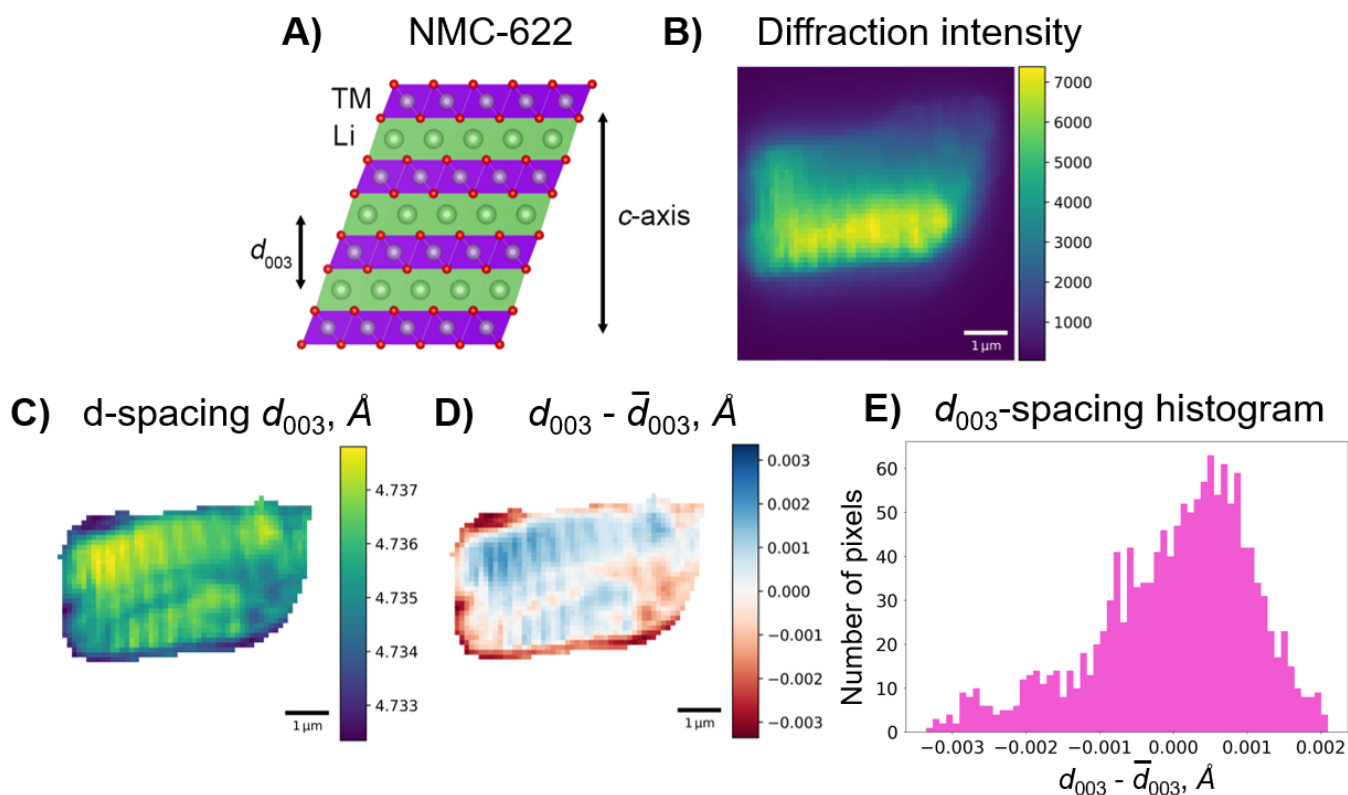
Figure 1: Scanning X-ray nanodiffraction microscopy of NMC-622 cathode single crystal. $LiNi_{0.6}Mn_{0.2}Co_{0.2}O_2$ crystal structure, showing the interlayer distance (d_{003}) between transition metal (purple) and Li (green) slabs probed by the diffraction imaging (A). Diffraction intensity map for a single crystal particle (B), calculated d-spacing map for the 003 reflection (C), difference between local and mean d-spacing for the measured crystallite. (D) Histogram of d-spacing values from the single crystal (E). The c-axis points out of plane in these images.

the NMC structure. The diffracted intensity map (Fig. 1B) is used to mask the image, so that only pixels where NMC is detected are fit. The d-spacing map of the particle is shown in Figure 1C. It is often more visually instructive to plot the d-spacing maps as differences from the mean value for the whole crystal, which allows areas of relative compressive and tensile strain to be easily detected (Fig. 1D). The histogram of the d-spacings is shown in Figure 1E, which represents the peak shape and width which would be observed using powder diffraction, considering only the one particle.

In these images we can observe stripe features in the c-axis of the particle. In addition, the outside of the particle exhibits a shorter c-axis than the inside of the particle. These stripe features bear a striking resemblance to the gliding planes recently described by Bi *et al.*.[14] Glide plane defects and periodic kinking have been re-ported in several high-resolution TEM studies on NMC.[14,20–22] Using the sodiated structure, Li *et al.* showed that this bending accumulates planar dislocations and kinks with a periodicity of $430\pm40\,nm$,[21] which is in excellent agreement with the *ca.* 440 nm period of the stripes in Figure 1C. These defects readily nucleate microcracks and irreversible phase transitions during charging and are responsible for capacity degradation of the active material.[21,23] In addition to creating lattice distortion, Lin *et al.* showed that these planar dislocations also induce Ni-Li antisite disordering, linked to structural instability.[22] Since the scattering power of Ni and Li are very different, local variation in site mixing may explain why the stripe features are also visible in the diffracted intensity map (Fig. 1B).

The peakshape of the histogram is asymmetrical, with a complex distribution that does not correspond to the typical Gaussian/Lorentzian
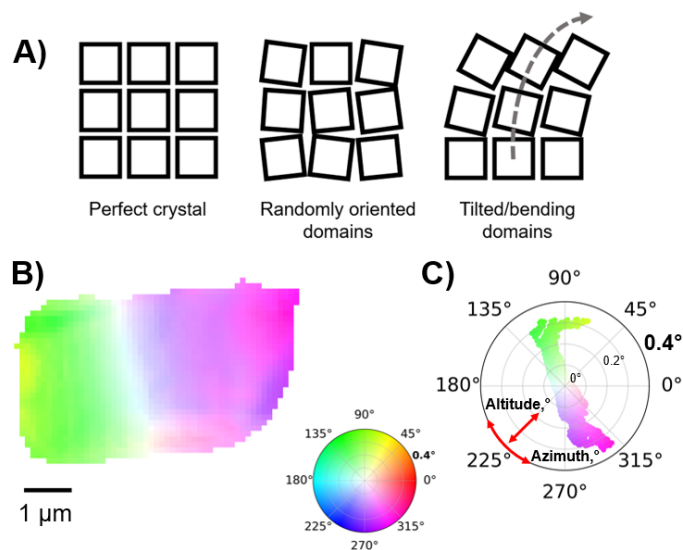
3

Figure 2: Scanning X-ray nanodiffraction microscopy of NMC-622 cathode single crystal. Illustration of random and bending mosaicity inside crystal structure, exaggerated for visibility (A). Crystal misorientation map (B). Misorientation pole figure scatter plot (C)

lineshapes usually considered in X-ray diffraction (Fig. 1E). The peak width of this histogram is known as microstrain ($\Delta d/d$, 4.2×10^{-4}), and is a useful parameter in evaluating the defectiveness of NMC.[11,24] Microstrain is normally considered a bulk parameter, but by using SXDM, it can be mapped across the particle by fitting the peak width of the diffraction pattern for each pixel (Fig. S2). This parameter offers a direct bridge between single particle measurements and more routine, accessible powder X-ray diffraction.

SXDM is highly sensitive to lattice tilt and orientation. Small rotations, tilts, bending, and geometric distortions of different domains inside the crystal are collectively referred to as mosaicity (Fig. 2A). Measurements of crystal mosaicity and orientation distributions at the nanoscale are still in their infancy. A variety of different approaches have emerged to probe this additional dimension of microstructural complexity with the necessary precision,[25–28] but a robust understanding of the origins and influence of mosaicity has not been established for battery materials.

The local rotation of the crystal lattice can either be directly mapped onto the crystal struc-

ture (Fig. 2B), or visualized in the form of a pole figure, where the direction and magnitude of the tilt are calculated in polar coordinates (Fig. 2C). Each point on the pole figure represents an identically colored pixel from the image in Figure 2B. The color varies continuously from one end of the crystallite to the other, indicating that there are no sharp discontinuities at the length scale of 100 nm. This pattern is characteristic of a crystal 'bending' in one direction perpendicular to the c-axis. While no striped features are visible in the tilt map, the bending is orthogonal to the direction of the stripes observed in the strain map.

The total curvature across the crystal is approximately 0.8°, which is orders of magnitude higher than the limit for purely elastic and continuous deformation, given the known rigidity and yield stress of NMC.[14,29] We can infer that at the atomic scale, a substantial quantity of defects are geometrically necessary to accommodate this distortion. The planar dislocations and antisite defects associated with bending and kinking in NMC are directly related to the formation of oxygen vacancies during crystal growth.[20] Oxygen is unstable inside the lattice at the high temperatures needed for growing single crystal Ni-rich materials, and strain/defects indicate incomplete control over the oxygen atmosphere and temperature used during synthesis. Plastic distortion and internal stress could also be introduced during milling and grinding processes,[30] which are sometimes applied between annealing steps to grow larger NMC crystals.[12]The precise synthetic route of the NMC analyzed here cannot be disclosed, which is a common limitation when evaluating state-of-the-art commercial battery materials.[11]

While SXDM allows structural heterogeneity at the intra-particle level to be discerned, it is always necessary to understand the inter-particle heterogeneity, and to what extent individual particles are representative of the bulk sample. To build a more statistically meaningful understanding of the sample microstructure, we imaged seven additional particles. The d-spacing and lattice tilt maps are shown in Figures 3A and 3B, respectively. The scattering
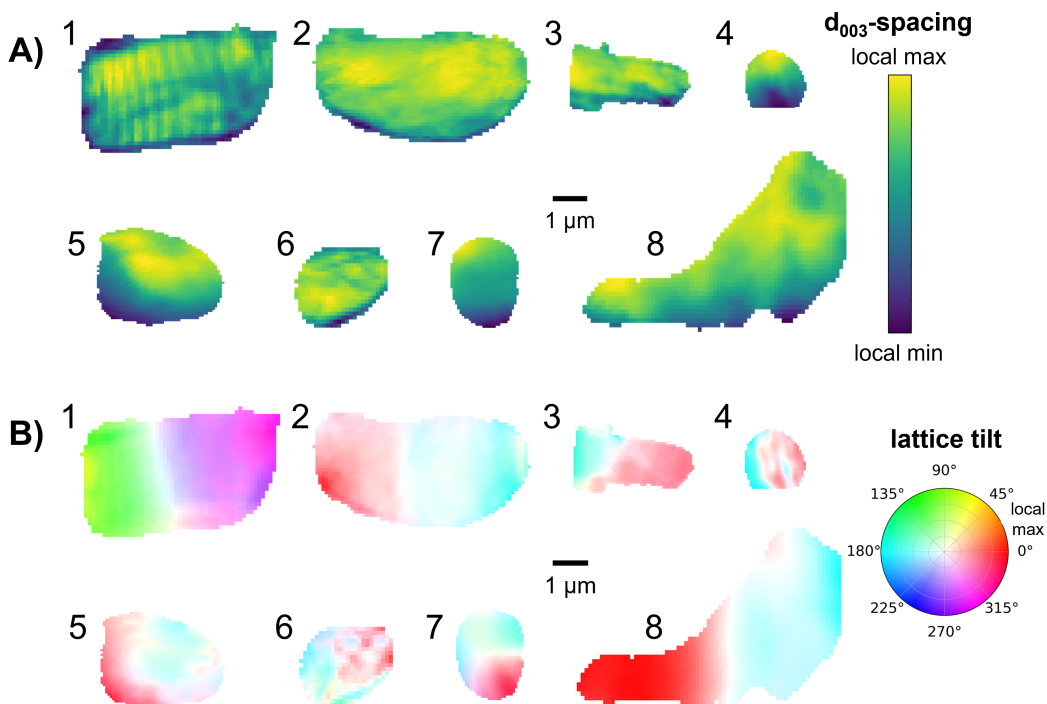
Figure 3: A) D-spacing maps of 8 different NMC-622 particles obtained from SXDM. The coloration is adjusted to span the range observed for each particle. B) Lattice tilt misorientation maps of the same NMC-622 particles obtained from SXDM.

intensity and d-spacing maps for each particle without normalization are displayed in Figure S3. The pole figures associated with Figure 3B are given in Figure S4.

The heterogeneity inside the sample is immediately apparent. All the measured crystals possess a mosaic structure, with sub-crystalline domains. There is a large distribution in size, shape, and internal morphology. Some particles are clearly part of fused, polycrystalline aggregates (3 and 8), but which share similar crystallographic orientation (Fig. S5. Each crystal has a unique internal strain gradient, ranging from particles 1 and 6 with complex internal nanostructure, to relatively featureless (2 and 7). Interestingly, particle 1 is the only crystal with an internal striped morphology. The orientation maps are similarly heterogeneous. The total curvature and the size of the crystallites are positively correlated (Fig. S6). Linear fitting of the ensemble of particles indicates that the crystals exhibit an average radius of curvature of $269 \pm 52\,\mathrm{um}$. Because crystallographic bending may reflect the presence of several types of defects which are difficult to distinguish, we propose the radius of curvature as a structural descriptor reflecting the quality of layered active materials. Less defective crystals by definition must exhibit less crystallographic curvature, independent of doping, transition metal stoichiometry, or mechanically induced distortion. Ongoing efforts to predict durability *ab initio* will need to account for these substantial deviations from the theoretical, unstrained, uncurved structure in order to accurately anticipate failure modes of micrometer sized crystals.[14]

The magnitude of this curvature is resolvable using modern electron backscatter diffraction (EBSD),[31] which is becoming more broadly available.[32] We anticipate that EBSD may be more convenient than SXDM for many researchers, considering recent improvements in speed and sensitivity, typically achieving $50\,\mathrm{nm}$ lateral resolution. However, EBSD can only measure the distortion within $20\,\mathrm{nm}$ of the surface, while SXDM images probe the thickness of the entire crystal. This depth summing effect renders the SXDM maps more representative of the total crystal microstructure, at the cost of

5

losing near-surface *vs* bulk information.

Phase Contrast X-ray Nano-tomography

Phase contrast tomography exploits the phase shift produced when a highly coherent X-ray beam interacts with the sample.[33] The use of a nano-sized beam and imaging at multiple sample-detector distances yields very high resolution images of sub-micro/micro-sized objects with excellent contrast. Following phase retrieval, the image intensities correspond approximately to the three-dimensional distribution of the object's electron density.[34] Nano-CT has several advantages over conventional FIB-SEM imaging. Despite lower ultimate spatial resolution, nano-CT can sample many hundreds or thousands of particles at once, which is essential for statistical representativeness. Additionally, it does not suffer from the need to prepare milled samples and therefore is non-destructive[35] However, beamtime at large scale facilities is typically required. The advent of 4th generation synchrotrons[36] has simultaneously improved the spatial resolution and acquisition time for nano-tomography, closing these competitive gaps.

A volume of $64\,\mu m \times 64\,\mu m \times 24\,\mu m$ of NMC powder has been systematically analysed, *i.e.* 3200 particles. Selected regions of interest inside the reconstructed volume displaying several NMC particles are shown in Figure 4. While many of the particles appear single crystal in nature (Fig. 4A,B), a significant fraction of polycrystalline material is also detected (Fig. 4C,D). The morphology of these particles is complex, and they appear to be 'welded' into porous aggregates, or have a faceted structure but with apparent porosity. The quantity of highly defective particles which exhibit inner pores, or an aggregated / welded structure, represents 17% of the total number of NMC particles imaged. The presence of these aggregates is evidence that the larger single crystals are formed through coalescence of smaller crystallites.

The morphology of the single crystal fraction of particles is typical of literature reports, and extended faceting is visible on the 3D views of particles **#1**, **#2** and **#3** (Fig. 4B). Faceted surfaces are also observable for particles **#4** and **#6** despite presenting inner morphological defects and pores. Globally, the particles display irregular shapes, which do not reflect the hexagonal unit cell of the NMC structure. In addition to flat facets, many of the crystals have rounded edges, or even concavity. In order to illustrate this, a detailed study of the morphology of the isolated particles is presented in Figure 5. By looking at the 3D rendering of a large population of NMC particles, it is possible to appreciate the diversity of the shape distribution (Fig. 5A). Therefore, several mathematical criteria have been considered to precisely quantify their geometry: the ellipticity, the sphericity and the roundness (summarized in Fig. S7).[37] First, the 3D ellipticity represents the elongation along its three spatial axes of the ellipsoid that fits the particle :

$$e_{yx} = \frac{b}{a}; e_{zx} = \frac{c}{a}; e_{zy} = \frac{c}{b}$$

The distribution of these elongations in 3D (Fig. 5B) appears to be very wide but not random and rather organized along a curved plane, which is indicative of the limited morphologies that can be adopted by these crystals. This indicates that particles have one or two preferential elongation directions. Furthermore, this distribution appears mostly independent of their equivalent sphere diameter, indicated by the size and color scale on the graph. For example, the largest particles exhibit anisotropic elongations, and particles aligned along the isotropic line (black line on the graph) display a wide range of equivalent diameter.

The size distribution of the particle's equivalent diameter ranges from $100\,nm$ up to $9.5\,\mu m$, with a median size of $1.9\,\mu m$, *i.e.* half of the powder volume is composed of the particles with an equivalent diameter smaller than this. Previous reports suggest that single crystals with a size between 1 and $4\,\mu m$ are sufficiently small to preserve (dis)charge rate capability in NMC.[38,39] The largest particles ($\leq 5\,\mu m$) represent more than $10\%^v$, which is non negligi-
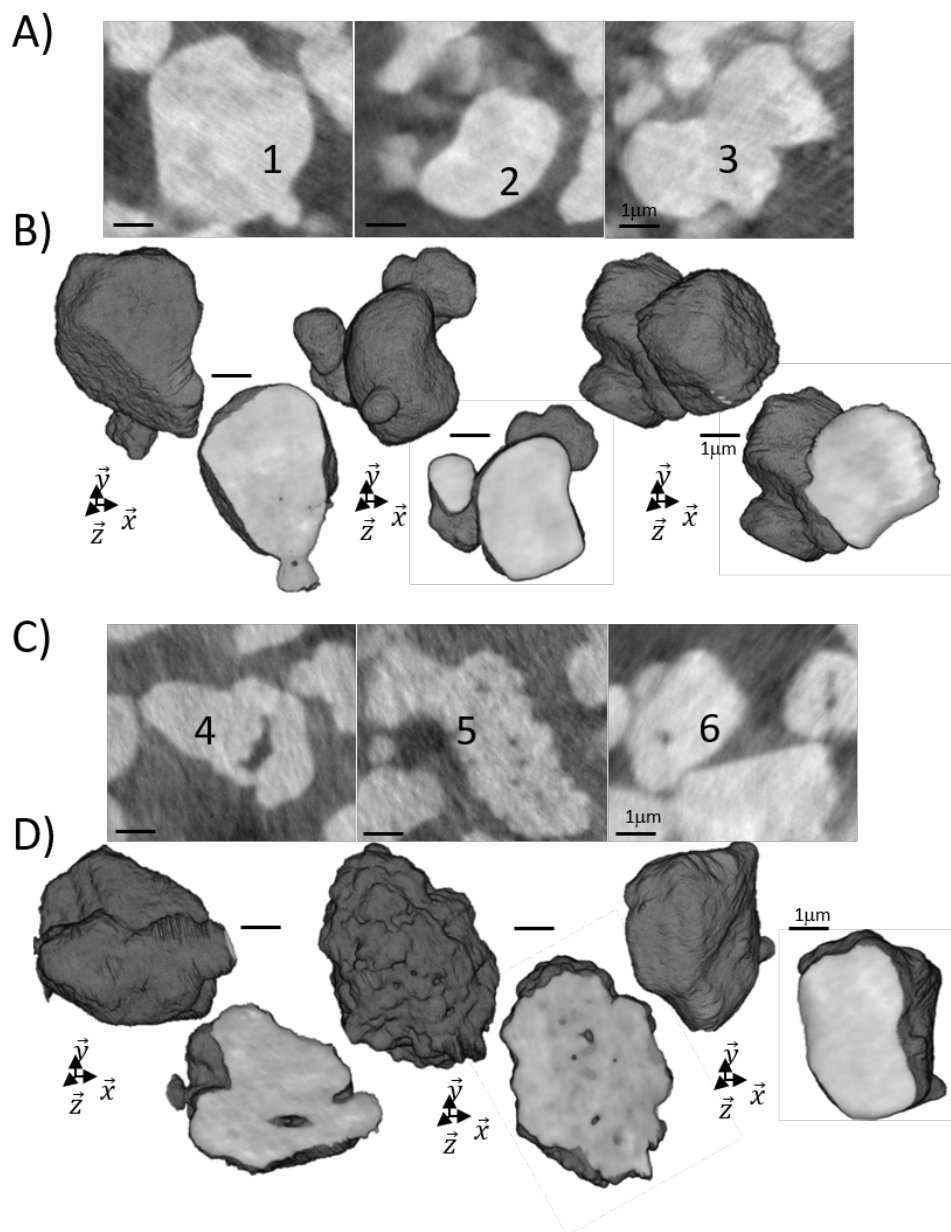
Figure 4: Nano-CT images of NMC-622 powder. A) Particles with faceted single crystals and C) polycrystalline, porous aggregate morphology are both observed. B) and D) are the respective 3D rendering views of the particles. The high greyscale levels correspond to the NMC particles and the low ones to the embedding epoxy and air. Scale bars are 1 um.

ble, and likely degrades the rate capability of the total active material. In addition, substantial volumes of large particles can have detrimental effects on the homogeneity of the electrode slurry deposition process, and electrode cohesion during cycling.[40,41] These parameters should therefore be carefully controlled during crystal growth.[24]

Shape is an important microstructural parameter, since it controls both the surface area to volume ratio, and often the crystallographic facets exposed on the particle surface, which are directly related to intercalation kinetics and degradation phenomena. The sphericity factor S, is the volume ratio of an inscribed sphere, which fits entirely within a particle, to the circumscribing sphere which encompasses the complete particle (Fig. S7B).[42] Given their respective radii, r_{ins} and r_{cir}, sphericity is defined as:
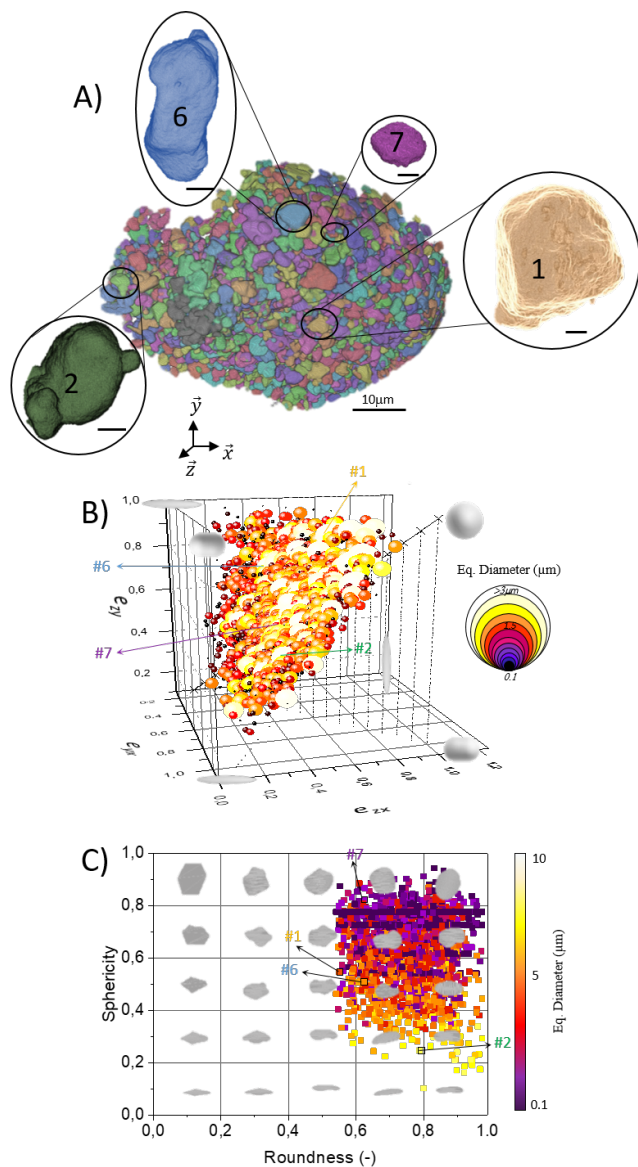
Figure 5: A) 3D rendering of the population of NMC particles isolated with three close-up views of the particle #1, #2 and #6 from figure 4. Scale bar is 10 and 1 μm for the large and small ones. B) Graph of the distribution of the 3D ellipticity for every single particle. The size and color-scale of the bubbles corresponds to the equivalent diameter of the fitting ellipsoid. C) Sphericity and roundness distribution for the population of particles and 3D rendering of the particles shape depending on their sphericity and roundness are represented in light grey.

$$S = \frac{r_{ins}}{r_{cir}}$$

The sphericity distribution of the NMC parti-

cle population has a median value of 0.67 (Fig. 5C), with a substantial fraction (45%) around 0.7-0.8. This makes the shape of the particles closer to the value of a cube (0.71) than a sphere. Their roundness R is defined as the ratio of the average radius of curvature of the corners of the object's silhouette to the radius of the maximum inscribed sphere[37,42] :

$$R = \frac{1}{n} \frac{\sum_i r_i}{r_{max}}$$

where n is the number of corners, r_i the radius of the ith corner curvature, and r_{max} the radius of the maximum inscribed circle (Fig. S7C). It is clear on the graph of the Figure 5C that most of the particles display a soft edge morphology [0.6-0.95], with a median roundness factor of 0.73 (Fig. 5C) compared to a cube geometry (0.53). Taken altogether, the morphology of the crystals are more of a 'potato-like' shape rather than a single crystal with sharp facets. Only a small number of particles (less than 15%) display surfaces with significant flatness than can be attributed to aligned crystallographic planes, *i.e.* with roundness between 0.5 and 0.6. More research is required to understand the relationship between crystal quality and particle shape, which is readily accessible from electron microscopy.

The ellipticity, sphericity and roundness for the four enclosed particles in Figure 5A (#6,#2,#1 and #7) as well as the median values obtained from the analysis of the entire population are summarized in Table S1. The particle #2 has a very high roundness for a low sphericity value, typical of an elongated ellipsoid morphology, compared to particle #1, which has the roundness of a square and the sphericity of a triangle. Globally, most of the particles have a geometry in between the ones of particle #6 and #2 as highlighted on the graph of Fig. 5C, whereas particle #1 belongs to the faceted-shape minority. The same trend is observed on smaller particles, as highlighted by the example of particle #7, with both large roundness and sphericity factor. Moreover, it is noticeable that the sphericity of particles decreases as their equivalent diameters increase, while keeping a high roundness factor (R $\geq$

8

0.6). These particle morphologies likely reflect the growth process of large NMC crystals through coalescence, and not growth kinetics along different crystallographic directions.

Contrast variation is visible inside the single crystal particles (Fig. 6). Two types of internal contrast variation could be observed, one with large amplitude and one with a much weaker shift in greyscale value. The smaller variations in greyscale value may be associated with local compositional heterogeneity of the Ni:Mn:Co ratio. Unfortunately, those variations are very close to the image background noise, and cannot be confidently assigned without higher resolution spectroscopic imaging. The larger contrast variation is apparent as dark spots inside the particle, and are attributed to internal porosity/voids, and/or microcracks inside the particles. Details concerning both sets of contrast variation are provided in the Supplementary Information. Some voids are clearly visible, and have well defined shapes (Fig. 6 red arrows). However, smaller voids, including microcracks $\leq 50\,$nm are incompletely resolved and present as heightened image noise. While previous investigations have shown that single crystals may contain a few microcracks or voids,[6,8] from these images it is clear that these voids can represent a significant volumetric fraction of the crystals.Depending on the particle selected and due to resolution limits , only 65-90% of the voids can be resolved (*i.e.* $\geq 50\,$nm). It is not possible to fully quantify this void volume fraction with certainty, but rather approximate its minimum value around 10% (Fig. S8).

The voids are not randomly dispersed through the particles, but can be highly clustered, such as in the middle of third particle in Figure 6B (red outline), where they are preferentially found in the middle of the crystallite. While the mechanism of void formation in NMC has been studied, the origin of void clustering remains unclear, and to the best of our knowledge has not been previously reported. One possible explanation is the formation of hollow structures during the growth process through the Kirkendall effect, and subsequent aggregation of these voids during annealing.[43,44] The transition metals quickly migrate outward to form the Li-rich active material, accompanied by slow diffusion of oxygen atoms inward, thus creating cavities inside of the particles. Substantial quantities of voids certainly reduces the theoretical volumetric energy density of the material, while remaining invisible on the surface. The larger clusters of voids may be associated with the microstructure seen in both lattice parameter and orientation maps. The individual voids are too small, and too numerous to be directly linked to the mosaicity detected with SXDM, emphasizing the complementarity of the techniques for characterizing this pristine material.

Voids almost certainly disrupt Li ion conduction, lowering the rate capability of the active material. Defects in single crystal cathode particles also serve as nucleation points for microcracks after long-term cycling. These defects and voids can to some extent be corrected by optimizing the crystal growth conditions inside the particles, and their subsequent annealing.[24] Long, high temperature annealing (up to 900 °C) is energetically expensive, creating a need for lower-temperature, faster growth conditions. If the temperature during synthesis and annealing is too high, evaporation of the Li salts and loss of oxygen also occur, drastically decreasing the structural stability and performance of the active material.[11,12] If the temperature is too low, then it becomes difficult to grow large, high-quality crystals. Therefore, tools which can quickly screen and evaluate the probable performance of the active material are valuable. Voids may even confer beneficial effects, by accommodating strain from anisotropic volumetric expansion, depending on the relative rate of different degradation phenomena. Degradation is a function of cycling parameters, and depends on specific device applications.[4] For example, an active material optimized for long-term cycling stability may require a different microstructure than for fast-charging,[45,46] or deep discharge.[8] Ultimately, the influence of these voids on performance and durability can only be validated using extended cycling, although we anticipate that the role of predictive analytics in cathode development will continue to grow over time.
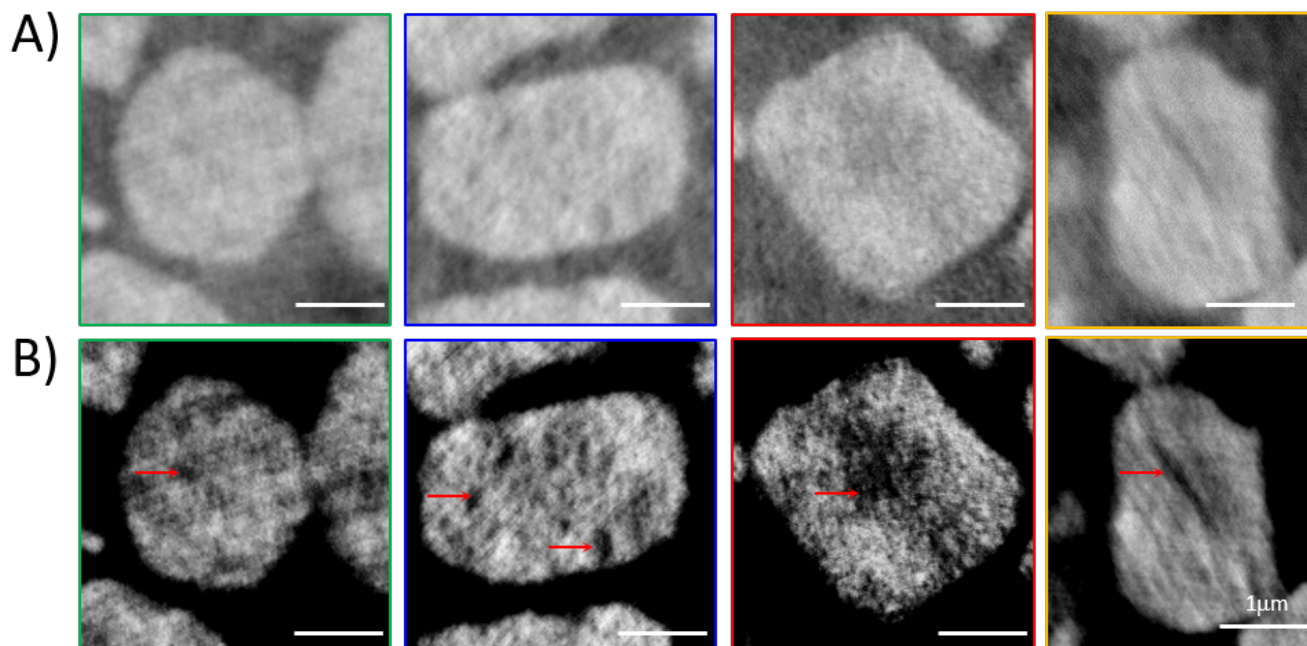
Figure 6: A) Close up view of some NMC particles and B) with contrast fixed on the greyscale values of the NMC particles only. Scale bar is 1 μm. Red arrows indicate the porosity/voids and/or microcracks inside the particles

Conclusions

Advanced characterization enables a deeper understanding of cathode microstructure, and can help explain not only the inter- and intra-particle heterogeneity, but also justify the range in reported performance for nominally identical NMC active materials. SXDM and nano-CT are demonstrated to be powerful probes for strain/tilt mosaicity, morphology, and internal voids in single crystal cathode materials. While the influence of these microstructural motifs must be thoroughly validated in actual devices, optimization and commercialization of these materials requires new heuristic tools which can predict the performance of active materials to guide their development. Layered active materials with higher nickel content are being aggressively pursued due to their higher energy density and lower cost. However, Ni-rich single crystals are even more difficult to manufacture, and we therefore expect these quality control issues to expand in the near term. Because both SXDM and nanoCT utilize hard X-rays, their *in situ* capabilities offer promising routes towards optimizing the annealing/synthesis of advanced cathode materials including NMC, and understanding degradation dynamics in operational cells. Recent advances in synchrotron microscopy allow these techniques to provide unprecedented insight towards the rational design of single crystal cathode active materials used in high performance lithium ion batteries.

Materials and Methods

NMC characterization

The $LiNi_{0.6}Mn_{0.2}Co_{0.2}O_2$ material used in this work was obtained from Umicore. Scanning X-ray nanodiffraction was collected at beamline ID01 at the European Synchrotron Radiation Facility. The X-ray wavelength was 1.24 Å, with a flux of 10^9 ph/s, focused using a Fresnel zone plate. The beam size was focused to a 140 nm spot for the particle in Figures 1 and 2, while the rest of the particles in 3 used a beam size of 80 nm. A 512 × 512 pixel Maxipix detector at a distance of 1.6 m was used to collect the nanodiffraction data. Detailed descriptions of the nanodiffraction microscope[19] and mapping technique[47] have been described previ-

10

ously. The stripe features shown in Figure 1 are not associated with linescan artifacts commonly observed in scanning probe microscopy.[48]

Nano-CT was performed at beamline ID16B[49] at the European Synchrotron Radiation Facility, using an X-ray beam with a photon energy of 29.6 keV. The nano-beam (50 nm × 50 nm) flux was 1.6 10^{12} ph/s. Four tomographies at four different distances from the focal plane were performed by acquiring 3203 projections over 360° with an exposure time of 0.04 s per projection recorded on a PCO edge 5.5 camera. The 3D reconstruction with a pixel size of 25 nm was achieved in two steps: (1) Recursive phase retrieval calculation[33,50] using an in-house developed octave script based on a Paganin-like approach with a delta/beta of 87 and (2) filtered back projection reconstruction using ESRF software PyHST2.[51] 32 to 8-bit conversion along with ring removal has been performed using a dedicated in-house developed Matlab script.

Image analysis

Image analyses were performed on the entire reconstructed volume using the ImageJ software package.[52] 3D renderings were made using the dedicated volume viewer plugin. Details on the procedures for the image segmentation and for their quantitative analyses (elongation, sphericity, roundness) are presented in the Supporting Information.

References

Supporting Information Available

Additional SXDM images, tomography, and electrochemical cycling data are available in Supporting Information file.

References

1. Ziegler, M. S.; Mueller, J. M.; Pereira, G. D.; Song, J.; Ferrara, M.; Chiang, Y.-M.; Trancik, J. E. Storage Requirements and Costs of Shaping Renewable Energy Toward Grid Decarbonization. *Joule* **2019**, *3*, 2134–2153.

2. Wang, Y.; Wang, E.; Zhang, X.; Yu, H. High-Voltage "Single-Crystal" Cathode Materials for Lithium-Ion Batteries. *Energy & Fuels* **2021**, *35*, 1918–1932.

3. Harlow, J. E.; Ma, X.; Li, J.; Logan, E.; Liu, Y.; Zhang, N.; Ma, L.; Glazier, S. L.; Cormier, M. M. E.; Genovese, M.; Buteau, S.; Cameron, A.; Stark, J. E.; Dahn, J. R. A Wide Range of Testing Results on an Excellent Lithium-Ion Cell Chemistry to be used as Benchmarks for New Battery Technologies. *Journal of The Electrochemical Society* **2019**, *166*, A3031–A3044.

4. Aiken, C. P.; Logan, E. R.; Eldesoky, A.; Hebecker, H.; Oxner, J. M.; Harlow, J. E.; Metzger, M.; Dahn, J. R. Li[Ni0.5Mn0.3Co0.2]O2 as a Superior Alternative to LiFePO4 for Long-Lived Low Voltage Li-Ion Cells. *Journal of The Electrochemical Society* **2022**, *169*, 050512, Publisher: The Electrochemical Society.

5. Langdon, J.; Manthiram, A. A Perspective on Single-Crystal Layered Oxide Cathodes for Lithium-Ion Batteries. *Energy Storage Materials* **2021**, *37*, 143–160.

6. Qian, G.; Zhang, Y.; Li, L.; Zhang, R.; Xu, J.; Cheng, Z.; Xie, S.; Wang, H.; Rao, Q.; He, Y.; Shen, Y.; Chen, L.;

Tang, M.; Ma, Z.-F. Single-Crystal Nickel-Rich Layered-Oxide Battery Cathode Materials: Synthesis, Electrochemistry, and Intra-Granular Fracture. *Energy Storage Materials* **2020**, *27*, 140–149.

7. Li, S.; Qian, G.; He, X.; Huang, X.; Lee, S.-J.; Jiang, Z.; Yang, Y.; Wang, W.-N.; Meng, D.; Yu, C.; Lee, J.-S.; Chu, Y. S.; Ma, Z.-F.; Pianetta, P.; Qiu, J.; Li, L.; Zhao, K.; Liu, Y. Thermal-healing of lattice defects for high-energy single-crystalline battery cathodes. *Nature Communications* **2022**, *13*, 704, Number: 1 Publisher: Nature Publishing Group.

8. Ryu, H.-H.; Namkoong, B.; Kim, J.-H.; Belharouak, I.; Yoon, C. S.; Sun, Y.-K. Capacity Fading Mechanisms in Ni-Rich Single-Crystal NCM Cathodes. *ACS Energy Letters* **2021**, *6*, 2726–2734.

9. Liu, Y.; Song, W.; Eldesoky, A.; Harlow, J.; Logan, E. R.; Li, H.; Dahn, J. R. The Impact of Upper Cut-Off Voltage on the Cycling Performance of Li-Ion Cells with Positive Electrodes Having Various Nickel Contents. *Journal of The Electrochemical Society* **2022**, *169*, 040531, Publisher: The Electrochemical Society.

10. Xu, C.; Merryweather, A. J.; Pandurangi, S. S.; Lun, Z.; Hall, D. S.; Deshpande, V. S.; Fleck, N. A.; Schnedermann, C.; Rao, A.; Grey, C. P. Operando visualization of kinetically induced lithium heterogeneities in single-particle layered Ni-rich cathodes. *Joule* **2022**, *6*, 2535–2546.

11. Liu, X.; Xu, G.-L.; Kolluru, V. S. C.; Zhao, C.; Li, Q.; Zhou, X.; Liu, Y.; Yin, L.; Zhuo, Z.; Daali, A.; Fan, J.-J.; Liu, W.; Ren, Y.; Xu, W.; Deng, J.; Hwang, I.; Ren, D.; Feng, X.; Sun, C.; Huang, L. *et al.* Origin and Regulation of Oxygen Redox Instability in High-Voltage Battery Cathodes. *Nature Energy* **2022**, 1–10.

12. Wang, T.; Ren, K.; He, M.; Dong, W.; Xiao, W.; Pan, H.; Yang, J.; Yang, Y.; Liu, P.; Cao, Z.; Ma, X.; Wang, H. Synthesis and Manipulation of Single-Crystalline Lithium Nickel Manganese Cobalt Oxide Cathodes: A Review of Growth Mechanism. *Frontiers in Chemistry* **2020**, *8*.

13. Paulsen, J.; Xia, X.; Han, S.-Y.; Zhang, J. Cathode Material for Rechargeable Solid State Lithium Ion Battery. 2017.

14. Bi, Y.; Tao, J.; Wu, Y.; Li, L.; Xu, Y.; Hu, E.; Wu, B.; Hu, J.; Wang, C.; Zhang, J.-G.; Qi, Y.; Xiao, J. Reversible Planar Gliding and Microcracking in a Single-Crystalline Ni-rich Cathode. *Science* **2020**, *370*, 1313–1317.

15. Wu, J.; Yang, Y.; Yang, W. Advances in soft X-ray RIXS for studying redox reaction states in batteries. *Dalton Transactions* **2020**, *49*, 13519–13527, Publisher: The Royal Society of Chemistry.

16. Ulvestad, U.; Singer, A.; Clark, J. N.; Cho, H. M.; Kim, J. W.; Harder, R.; Maser, J.; Meng, Y. S.; Shpyrko, O. G. Topological defect dynamics in operando battery nanoparticles. *Science* **2015**, *348*, 1344–1347.

17. Lin, F.; Liu, Y.; Yu, X.; Cheng, L.; Singer, A.; Shpyrko, O. G.; Xin, H. L.; Tamura, N.; Tian, C.; Weng, T.-C.; Yang, X.-Q.; Meng, Y. S.; Nordlund, D.; Yang, W.; Doeff, M. M. Synchrotron X-ray Analytical Techniques for Studying Materials Electrochemistry in Rechargeable Batteries. *Chemical Reviews* **2017**, *117*, 13123–13186.

18. Chahine, G. A.; Richard, M.-I.; Homs-Regojo, R. A.; Tran-Caliste, T. N.; Carbone, D.; Jacques, V. L. R.; Grifone, R.; Boesecke, P.; Katzer, J.; Costina, I.; Djazouli, H.; Schroeder, T.; Schülli, T. U. Imaging of strain and lattice orientation by quick scanning X-ray microscopy combined with three-dimensional reciprocal space mapping. *Journal of Applied Crystallography* **2014**, *47*, 762–769.

19. Leake, S. J.; Chahine, G. A.; Djazouli, H.; Zhou, T.; Richter, C.; Hilhorst, J.; Petit, L.; Richard, M. I.; Morawe, C.; Barrett, R.; Zhang, L.; Homs-Regojo, R. A.; Favre-Nicolin, V.; Boesecke, P.; Schülli, T. U. The nanodiffraction beamline ID01/ESRF: A microscope for imaging strain and structure. *Journal of Synchrotron Radiation* **2019**, *26*, 571–584.

20. Meng, X.-H.; Lin, T.; Mao, H.; Shi, J.-L.; Sheng, H.; Zou, Y.-G.; Fan, M.; Jiang, K.; Xiao, R.-J.; Xiao, D.; Gu, L.; Wan, L.-J.; Guo, Y.-G. Kinetic Origin of Planar Gliding in Single-Crystalline Ni-Rich Cathodes. *Journal of the American Chemical Society* **2022**, *144*, 11338–11347, Publisher: American Chemical Society.

21. Li, Y.; Li, X.; Du, C.; Sun, H.; Zhang, Y.; Liu, Q.; Yang, T.; Zhao, J.; Delmas, C.; Harris, S. J.; Chen, H.; Huang, Q.; Tang, Y.; Zhang, L.; Zhu, T.; Huang, J. Degradation by Kinking in Layered Cathode Materials. *ACS Energy Letters* **2021**, *6*, 3960–3969, Publisher: American Chemical Society.

22. Lin, Q.; Guan, W.; Zhou, J.; Meng, J.; Huang, W.; Chen, T.; Gao, Q.; Wei, X.; Zeng, Y.; Li, J.; Zhang, Z. Ni–Li anti-site defect induced intragranular cracking in Ni-rich layer-structured cathode. *Nano Energy* **2020**, *76*, 105021.

23. Zhang, H.; Omenya, F.; Yan, P.; Luo, L.; Whittingham, M. S.; Wang, C.; Zhou, G. Rock-Salt Growth-Induced (003) Cracking in a Layered Positive Electrode for Li-Ion Batteries. *ACS Energy Letters* **2017**, *2*, 2607–2615.

24. Li, S.; Qian, G.; He, X.; Huang, X.; Lee, S.-J.; Jiang, Z.; Yang, Y.; Wang, W.-N.; Meng, D.; Yu, C.; Lee, J.-S.; Chu, Y. S.; Ma, Z.-F.; Pianetta, P.; Qiu, J.; Li, L.; Zhao, K.; Liu, Y. Thermal-healing of lattice defects for high-energy single-crystalline battery cathodes. *Nature Communications* **2022**, *13*, 704, Number: 1 Publisher: Nature Publishing Group.

25. Purohit, R. R. P. P. R.; Tardif, S.; Castelnau, O.; Eymery, J.; Guinebretière, R.; Robach, O.; Ors, T.; Micha, J.-S. LaueNN: neural-network-based *hkl* recognition of Laue spots and its application to polycrystalline materials. *Journal of Applied Crystallography* **2022**, *55*, 737–750.

26. Rauch, E. F.; Véron, M. Automated crystal orientation and phase mapping in TEM. *Materials Characterization* **2014**, *98*, 1–9.

27. Carnis, J.; Gao, L.; Labat, S.; Kim, Y. Y.; Hofmann, J. P.; Leake, S. J.; Schülli, T. U.; Hensen, E. J.; Thomas, O.; Richard, M. I. Towards a quantitative determination of strain in Bragg Coherent X-ray Diffraction Imaging: artefacts and sign convention in reconstructions. *Scientific Reports* **2019**, *9*, 17357.

28. Li, J.; Hong, Y.; Yan, H.; Chu, Y. S.; Pianetta, P.; Li, H.; Ratner, D.; Huang, X.; Yu, X.; Liu, Y. Probing lattice defects in crystalline battery cathode using hard X-ray nanoprobe with data-driven modeling. *Energy Storage Materials* **2022**, *45*, 647–655.

29. Singer, A.; Zhang, M.; Hy, S.; Cela, D.; Fang, C.; Wynn, T. A.; Qiu, B.; Xia, Y.; Liu, Z.; Ulvestad, A.; Hua, N.; Wingert, J.; Liu, H.; Sprung, M.; Zozulya, A. V.; Maxey, E.; Harder, R.; Meng, Y. S.; Shpyrko, O. G. Nucleation of dislocations and their dynamics in layered oxide cathode materials during battery charging. *Nature Energy* **2018**, *3*, 641–647.

30. Pan, T.; Alvarado, J.; Zhu, J.; Yue, Y.; Xin, H. L.; Nordlund, D.; Lin, F.; Doeff, M. M. Structural Degradation of Layered Cathode Materials in Lithium-Ion Batteries Induced by Ball Milling. *Journal of The Electrochemical Society* **2019**, *166*, A1964, Publisher: IOP Publishing.

31. Plancher, E.; Petit, J.; Maurice, C.; Favier, V.; Saintoyant, L.; Loisnard, D.; Rupin, N.; Marijon, J.-B.; Ulrich, O.; Bornert, M.; Micha, J.-S.; Robach, O.;

Castelnau, O. On the Accuracy of Elastic Strain Field Measurements by Laue Microdiffraction and High-Resolution EBSD: a Cross-Validation Experiment. *Experimental Mechanics* **2016**, *56*, 483–492.

32. Wilkinson, A. J.; Britton, T. B.; Jiang, J.; Karamched, P. S. A review of advances and challenges in EBSD strain mapping. *IOP Conference Series: Materials Science and Engineering* **2014**, *55*, 012020.

33. Cloetens, P.; Ludwig, W.; Baruchel, J.; Van Dyck, D.; Van Landuyt, J.; Guigay, J. P.; Schlenker, M. Holotomography: Quantitative phase tomography with micrometer resolution using hard synchrotron radiation x rays. *Applied Physics Letters* **1999**, *75*, 2912–2914.

34. Zabler, S.; Cloetens, P.; Guigay, J.-P.; Baruchel, J.; Schlenker, M. Optimization of phase contrast imaging using hard x rays. *Review of Scientific Instruments* **2005**, *76*, 073705.

35. Kim, S.-H.; Antonov, S.; Zhou, X.; Stephenson, L. T.; Jung, C.; El-Zoka, A. A.; Schreiber, D. K.; Conroy, M.; Gault, B. Atom probe analysis of electrode materials for Li-ion batteries: challenges and ways forward. *Journal of Materials Chemistry A* **2022**, *10*, 4926–4935, Publisher: The Royal Society of Chemistry.

36. Raimondi, P. ESRF-EBS: The Extremely Brilliant Source Project. *Synchrotron Radiation News* **2016**, *29*, 8–15, Publisher: Taylor & Francis.

37. Zhao, B.; Wang, J. 3D quantitative shape analysis on form, roundness, and compactness with μCT. *Powder Technology* **2016**, *291*, 262–275.

38. Kimijima, T.; Zettsu, N.; Teshima, K. Growth Manner of Octahedral-Shaped Li(Ni1/3Co1/3Mn1/3)O2 Single Crystals in Molten Na2SO4. *Crystal Growth & Design* **2016**, *16*, 2618–2623.

39. Wang, L.; Wu, B.; Mu, D.; Liu, X.; Peng, Y.; Xu, H.; Liu, Q.; Gai, L.; Wu, F. Single-crystal LiNi0.6Co0.2Mn0.2O2 as high performance cathode materials for Li-ion batteries. *Journal of Alloys and Compounds* **2016**, *674*, 360–367.

40. Teichert, P.; Eshetu, G. G.; Jahnke, H.; Figgemeier, E. Degradation and Aging Routes of Ni-Rich Cathode Based Li-Ion Batteries. *Batteries* **2020**, *6*.

41. David, L.; Ruther, R. E.; Mohanty, D.; Meyer, H. M.; Sheng, Y.; Kalnaus, S.; Daniel, C.; Wood, D. L. Identifying degradation mechanisms in lithium-ion batteries with coating defects at the cathode. *Applied Energy* **2018**, *231*, 446–455.

42. Wadell, H. Volume, Shape, and Roundness of Rock Particles. *The Journal of Geology* **1932**, *40*, 443–451.

43. Li, S.; Yao, Z.; Zheng, J.; Fu, M.; Cen, J.; Hwang, S.; Jin, H.; Orlov, A.; Gu, L.; Wang, S.; Chen, Z.; Su, D. Direct Observation of Defect-Aided Structural Evolution in a Nickel-Rich Layered Cathode. *Angewandte Chemie International Edition* **2020**, *59*, 22092–22099.

44. Pimenta, V.; Sathiya, M.; Batuk, D.; Abakumov, A. M.; Giaume, D.; Cassaignon, S.; Larcher, D.; Tarascon, J.-M. Synthesis of Li-Rich NMC: A Comprehensive Study. *Chemistry of Materials* **2017**, *29*, 9923–9936.

45. Wang, R.; Chen, X.; Huang, Z.; Yang, J.; Liu, F.; Chu, M.; Liu, T.; Wang, C.; Zhu, W.; Li, S.; Li, S.; Zheng, J.; Chen, J.; He, L.; Jin, L.; Pan, F.; Xiao, Y. Twin boundary defect engineering improves lithium-ion diffusion for fast-charging spinel cathode materials. *Nature Communications* **2021**, *12*, 3085, Number: 1 Publisher: Nature Publishing Group.

46. Ren, D.; Padgett, E.; Yang, Y.; Shen, L.; Shen, Y.; Levin, B. D. A.; Yu, Y.; DiSalvo, F. J.; Muller, D. A.; Abruña, H. D.

Ultrahigh Rate Performance of a Robust Lithium Nickel Manganese Cobalt Oxide Cathode with Preferentially Orientated Li-Diffusing Channels. *ACS Applied Materials & Interfaces* **2019**, *11*, 41178–41187.

47. Chahine, G. A.; Richard, M. I.; Homs-Regojo, R. A.; Tran-Caliste, T. N.; Carbone, D.; Jaques, V. L. R.; Grifone, R.; Boesecke, P.; Katzer, J.; Costina, I.; Djazouli, H.; Schroeder, T.; Schülli, T. U. Imaging of strain and lattice orientation by quick scanning X-ray microscopy combined with three-dimensional reciprocal space mapping. *Journal of Applied Crystallography* **2014**, *47*, 762–769.

48. Cesbron, Y.; Shaw, C. P.; Birchall, J. P.; Free, P.; Lévy, R. Stripy Nanoparticles Revisited. *Small* **2012**, *8*, 3714–3719.

49. Martínez-Criado, G.; Villanova, J.; Tucoulou, R.; Salomon, D.; Suuronen, J.-P.; Labouré, S.; Guilloud, C.; Valls, V.; Barrett, R.; Gagliardini, E.; Dabin, Y.; Baker, R.; Bohic, S.; Cohen, C.; Morse, J. ID16B: a hard X-ray nanoprobe beamline at the ESRF for nano-analysis. *Journal of Synchrotron Radiation* **2016**, *23*, 344–352.

50. Langer, M.; Pacureanu, A.; Suhonen, H.; Grimal, Q.; Cloetens, P.; Peyrin, F. X-Ray Phase Nanotomography Resolves the 3D Human Bone Ultrastructure. *PLOS ONE* **2012**, *7*, 1–7.

51. Mirone, A.; Brun, E.; Gouillart, E.; Tafforeau, P.; Kieffer, J. The PyHST2 hybrid distributed code for high speed tomographic reconstruction with iterative reconstruction and a priori knowledge capabilities. *Nuclear Instruments and Methods in Physics Research Section B: Beam Interactions with Materials and Atoms* **2014**, *324*, 41–48, 1st International Conference on Tomography of Materials and Structures.

52. Schindelin, J.; Arganda-Carreras, I.; Frise, E.; Kaynig, V.; Longair, M.; Pietzsch, T.; Preibisch, S.; Rueden, C.; Saalfeld, S.; Schmid, B.; Tinevez, J.-Y.; White, D. J.; Hartenstein, V.; Eliceiri, K.; Tomancak, P.; Cardona, A. Fiji: an open-source platform for biological-image analysis. *Nature Methods* **2012**, *9*, 676–682.

TOC Graphic

Some journals require a graphical entry for the Table of Contents. This should be laid out "print ready" so that the sizing of the text is correct. Inside the `tocentry` environment, the font used is Helvetica 8 pt, as required by *Journal of the American Chemical Society*.

The surrounding frame is 9 cm by 3.5 cm, which is the maximum permitted for *Journal of the American Chemical Society* graphical table of content entries. The box will not resize if the content is too big: instead it will overflow the edge of the box.

This box and the associated title will always be printed on a separate page at the end of the document.

Supporting Information:

Imaging voids and defects inside Li-ion cathode LiNi$_{0.6}$Mn$_{0.2}$Co$_{0.2}$O$_2$ single crystals

Isaac Martens,[†] Victor Vanpeene,[†,‡] Nikita Vostrov,[†] Steven Leake,[†] Edoardo Zatterin,[†] Jeremie Auvergniot,[¶] Jakub Drnec,[†] Marie-Ingrid Richard,[†,§] Julie Villanova,[*,†] and Tobias Schulli[*,†]

[†]*European Synchrotron Radiation Facility, 71 Avenue des Martyrs, Grenoble 38000, France*

[‡]*Université Grenoble Alpes, CEA Grenoble, LITEN, 17 rue des Martyrs, 38054 Grenoble, France*

[¶]*Umicore, France*

[§]*Univ. Grenoble Alpes, CEA Grenoble, IRIG, MEM, NRX, 17 rue des Martyrs 38000 Grenoble, France*

E-mail: villanova@esrf.fr; schulli@esrf.fr

SXDM data analysis

Python scripts in combination with the XSOCS library developed at ESRF (https://kmap.gitlab-pages.esrf.fr/xsocs/) were used to analyse the data. Conversion of the diffracted intensities to reciprocal space maps was performed by binning the diffraction data in each voxel of a array with dimensions of 50x100x100 and applying a 2x2 median filter. 3D center of mass fitting of the Bragg peak was used to determine the direction and the length of local Q-space vectors. The threshold parameter used for masking the particle area was equal to 20% of
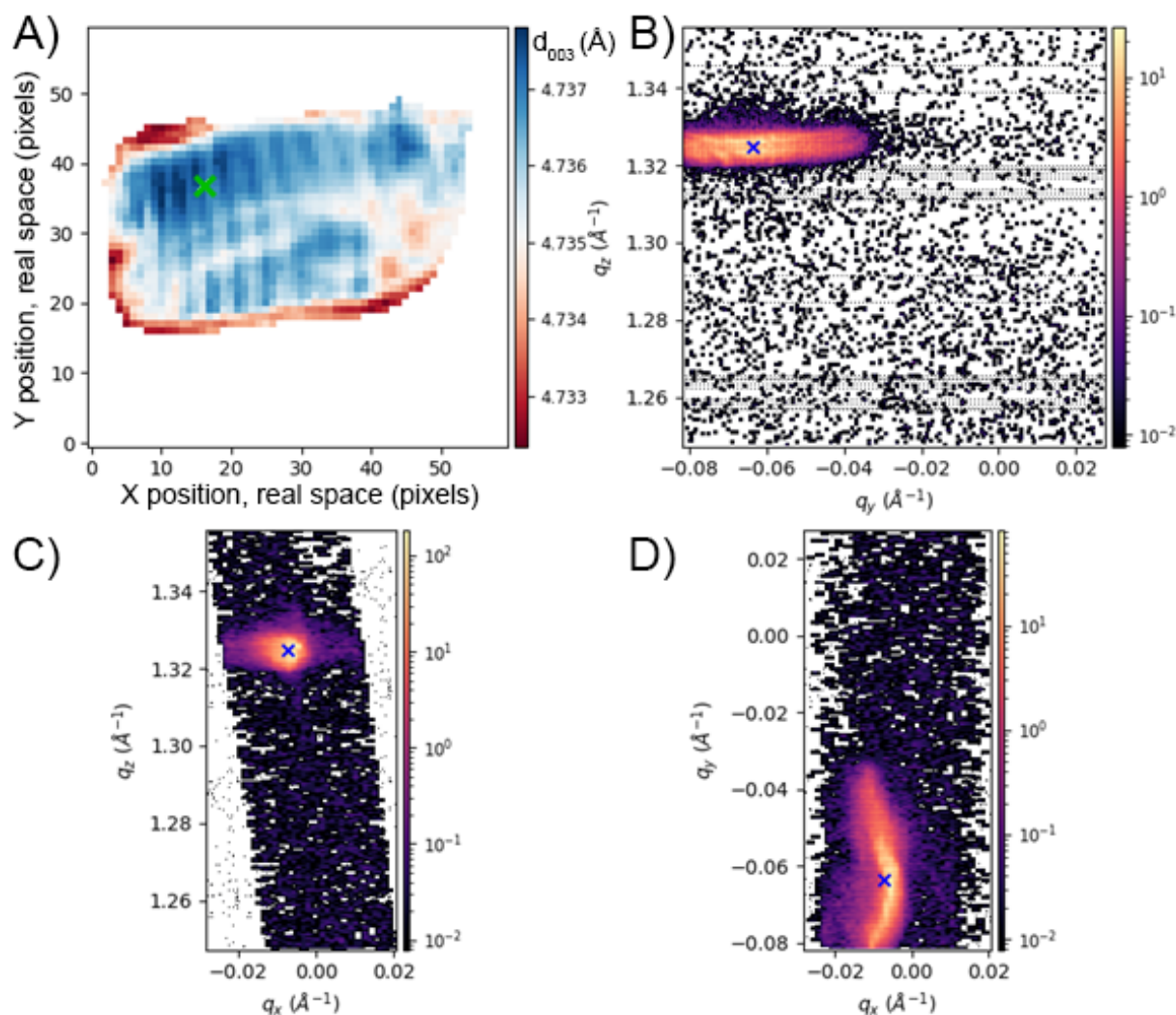
the maximum for all scans.

Figure S1: Example of 5 dimensional SXDM dataset corresponding to the particle in Figures 1 and 2 of the main text. D-spacing map of the particle, with a green X indicating the pixel plotted in reciprocal space (A). 3D reciprocal space maps sliced through the YZ (B), XZ (C), and XY (D) planes. Blue Xs mark the fitted center of mass peak position in 3D.

Figure S1 shows an subset of the 5D dataset obtained from SXDM. Each pixel of the 2D map has a 3D reciprocal space map of the diffraction data. The signal from a selected pixel of the real space map is shown in three projections through reciprocal space. The peak position and width in all three dimensions can be fit and analyzed. In this coordinate system, X is the rocking curve direction, Y is the direction along the powder ring, and Z is the scattering angle 2θ. Z contains the d-spacing information typically measured in powder

diffraction, while X and Y relate the orientation of the crystal lattice. Qyz corresponds to a single detector frame.
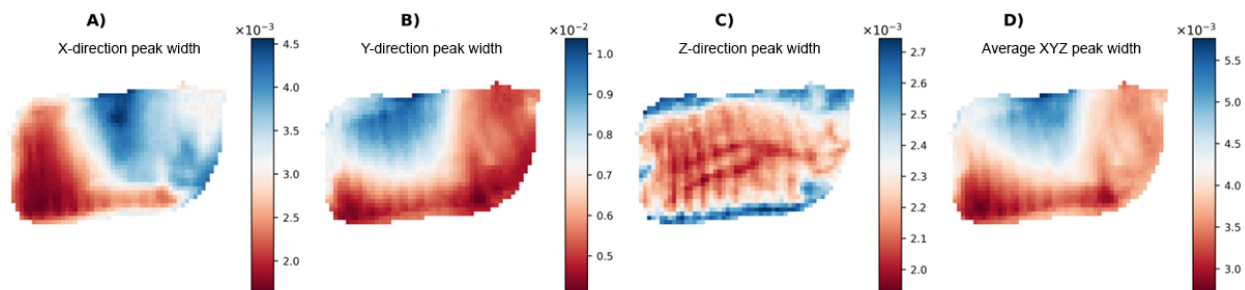

Figure S2: Peak width maps obtained from fitting the diffraction peak of the particle in all three reciprocal space directions.

Figures 1 and 2 of the main text show the peak position and direction of the lattice. Figure S2 shows the equivalent map with peak widths, after fitting with a Gaussian lineshape. The X and Y direction reflect the local curvature of the lattice, while the Z direction corresponds to the local microstrain. No correction for the convolution of sample related broadening with instrumental divergence of the focused beam was made, so the calculated microstrain slightly overestimates the true values. Nevertheless, the sample-induced broadening was much higher than the instrumental contributions.

The d-spacing maps for particles 2 through 7 without normalization are shown in Figure S3. The pole figures corresponding to all the crystals shown in Figure 3 are provided in Figure S4.

While fused together and overlapping in the real space image, several individual sub-crystalline domains composing particle 8 could be isolated by examining slight differences in their local orientation (Fig. S5). This strategy allows crystal coalescence mechanisms to be studied in detail. All particles in this figure originate from a single SXDM dataset. In Figure S5A, the XRD intensity, d-spacing map and tilt map for the larger particle 8 is given. Parts B and C represent the left and right hand side of the particle, which exhibit slightly different orientations and d-spacings. In addition to the large particle, there are numerous smaller crystallites surrounding it which overlap in the real space image, but which can be
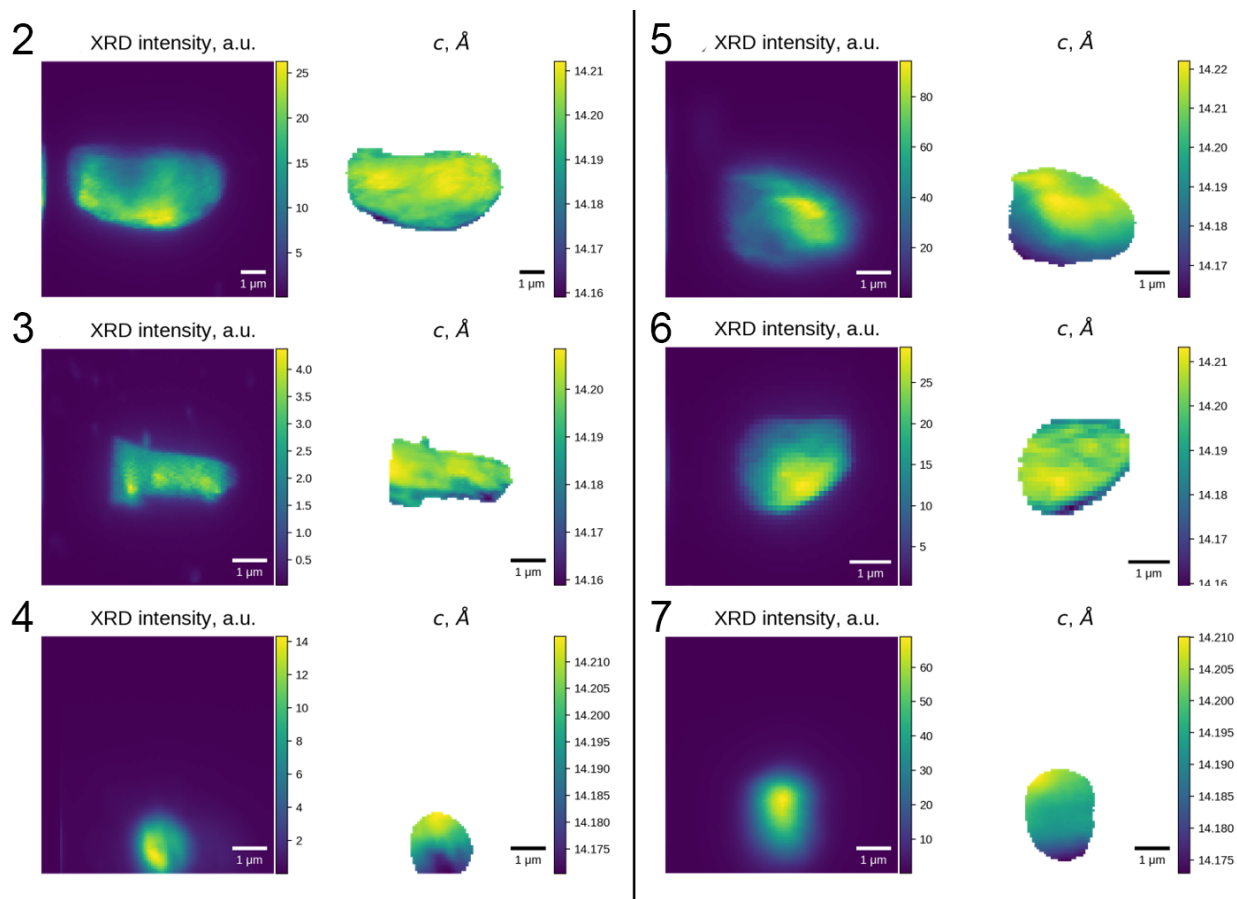
Figure S3: Intensity and d-spacing maps for particles 2-8, corresponding to the same images seen in Figure 3 of the main text.

decovoluted through orientation. All of these crystallites possess different strains and strain distributions, which is evident in the different shapes of their d-spacing histograms.

The radius of curvature for the crystals can be calculated by examining the size of crystal, and the total lattice tilt observed along the same axis. Using particle 3 as an example, the crystal is approximately 4.3 µm between the most intensely red and blue colored regions. Instead of mapping the tilt values onto the real space image of the particle, the magnitude and direction of the tilt can be displayed as a pole figure. Using the pole figure we can see that the particle is strongly bent along a single axis, with a total curvature of 0.51 deg. Plotting the size and curvature of all the crystals allows for determining the average radius of curvature, which was performed using a linear fit. Particle 4 was omitted, because the peak stretched off the edge of the detector and the total curvature could not be reliably calculated.
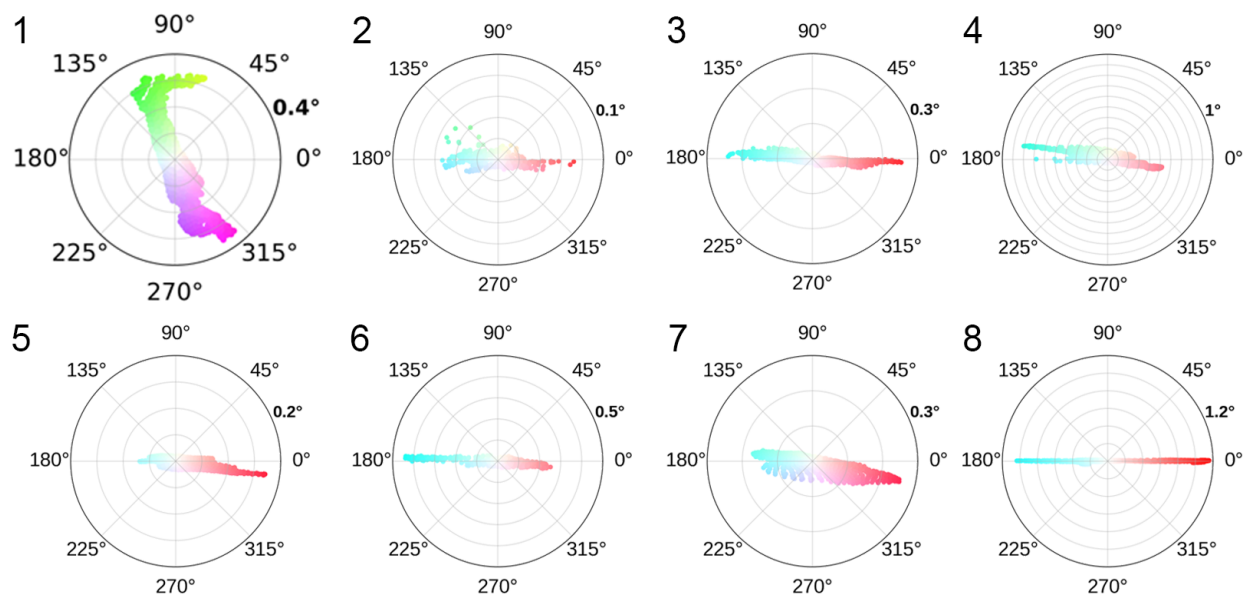
Figure S4: Altitude/azimuth orientation pole figures for the 8 particles imaged with SXDM.

Note that the goodness of the fit in this relationship is not determined by the quality of the SXDM analysis, but rather the heterogeneity in the defect content of crystallites in the sample.

It may be noticed that in the tilt orientation maps all the particles are colored red-blue (with the exception of particle 1) and their tilts preferentially oriented east-west along the polar coordinate system. Randomly oriented particles in a powder do not show any preference. This is an artifact resulting from how the initial crystallite search was performed, by imaging a large 2D slice of reciprocal space with low spatial resolution, followed by measuring selected crystals in 3D with higher resolution. Strongly diffracting particles selected for measurement are therefore aligned with the initial search vector. This axis has no special significance, and physically rotating the sample by 90 deg would align the bending of the particles into the north-south orientation. However, because the reciprocal space maps are sampled with better resolution in the detector plane than the rocking curve direction, this methodology produces much higher quality SXDM maps in shorter acquisition times, and reduces susceptibility to drift.
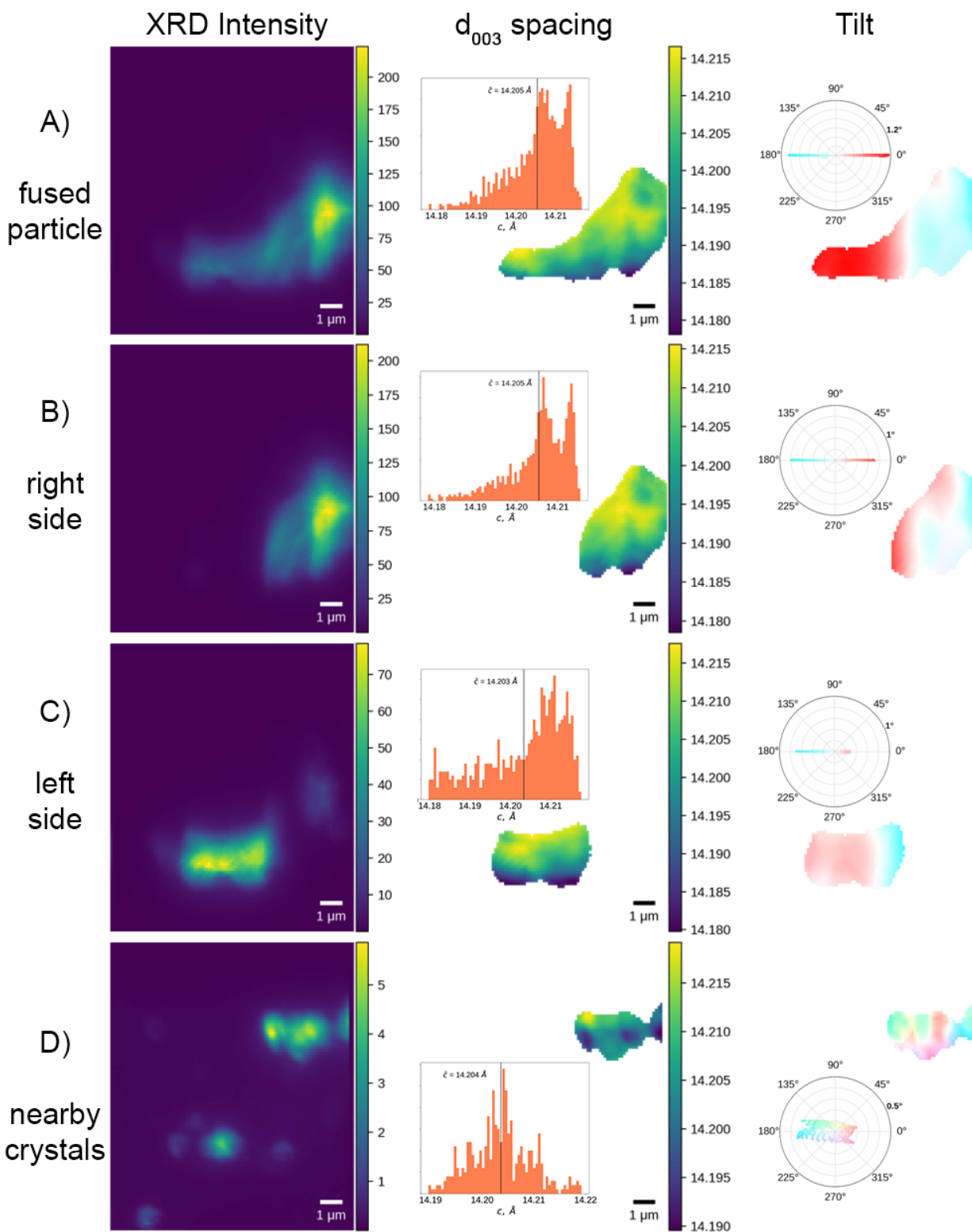
S-5

Figure S5: Decomposition of a single SXDM dataset containing particle 8 into sub-crystallite domains, organized by XRD intensity maps, local d-spacing (with inset histograms) and tilt maps.
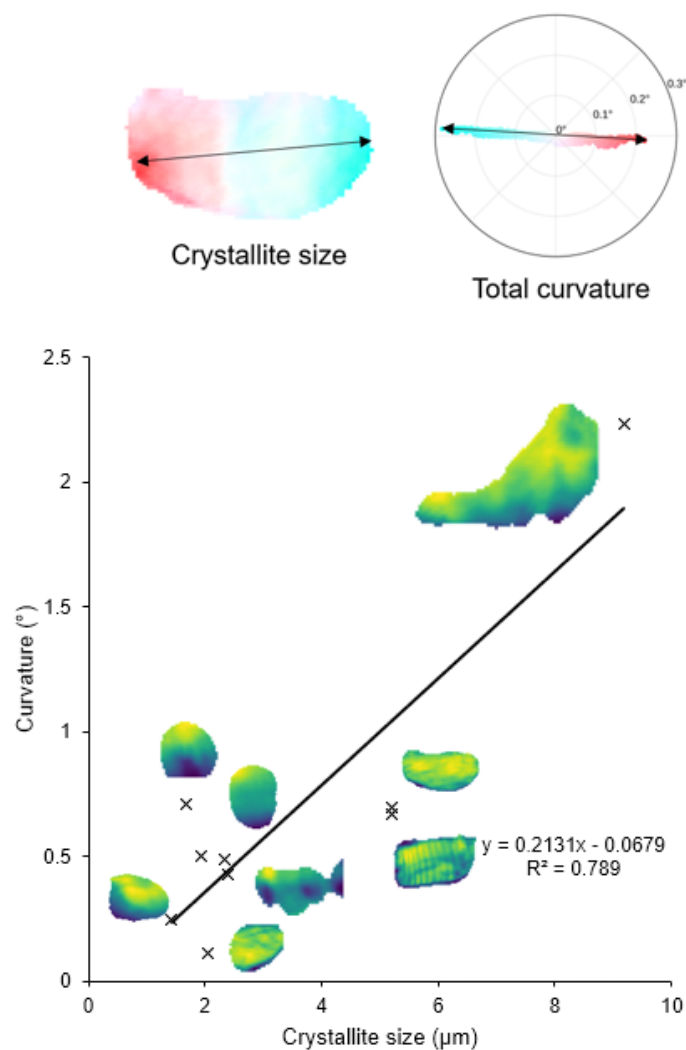
Figure S6: Relationship between total curvature of the NMC crystals and size of the crystal, calculated using the tilt maps of each particle as labelled.

X-ray nanotomography

Image analyses were performed on the 8-bit ring filtered images using the ImageJ software [1]. The images display three principal grey scale level, the brightest corresponds to the NMC particles, and the intermediate grey to the glue used for fixing the particle on top of the glass capillary. The lowest grey value (dark) corresponds to pores filled with air. The segmentation of the phase of interest (NMC) is performed using thresholding on a fixed value, which was estimated from the deconvolution of the grey value histogram by the means of the

multi-peak fitting tool of the OriginPro software [2]. After segmentation, binary 3D images of the NMC particles were refined through watershed and labelling using ImageJ operation for attributing separated grey value to every single particle. The isolated particles are then used for quantitative analysis of their morphological characteristics. The volume and surface of each particles are measured using a marching cube algorithm [3] and inertia ellipsoid are used to fit the particles. The 3D ellipticity represents the elongation along its three spatial axis of the ellipsoid that fits the particle, such as Fig.S7A:

$$e_{yx} = \frac{b}{a}; e_{zx} = \frac{c}{a}; e_{zy} = \frac{c}{b}$$

Their sphericity S is a function of the volume ratio of the reference sphere to the circumscribing one (Fig.S7B), with r_{ins} and r_{cir} their respective radius:

$$S = \frac{r_{ins}}{r_{cir}}$$

Their roundness R is defined as the ratio of the average radius of curvature of the corners of the object's silhouette to the radius of the maximum inscribed sphere:

$$R = \frac{1}{n} \frac{\sum_i r_i}{r_{max}}$$

where n is the number of corners, r_i the radius of the ith corner curvature, and $rmax$ the radius of the maximum inscribed circle (Fig.S7C).

Table S1: Morphological parameters of the three particles of Figure 5A compared to the global NMC particles population

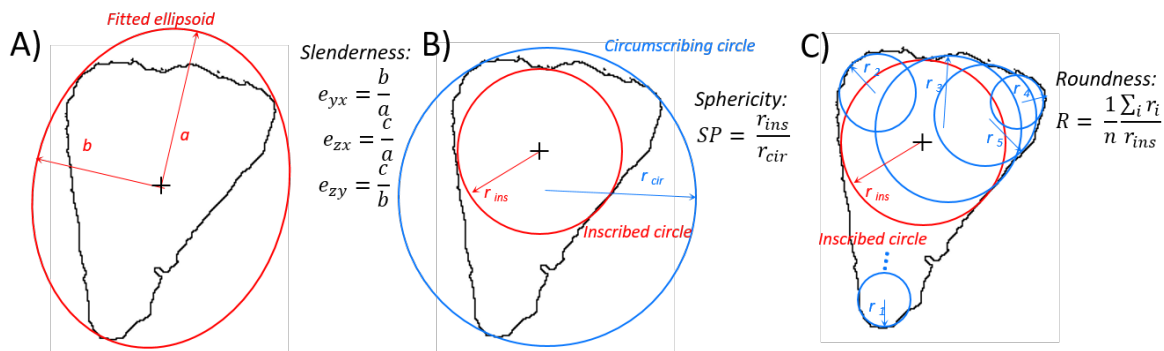| Particle	Eq. diam. (μm)	e_{yx}	e_{zx}	e_{zy}	S	R
#6	3.26	0.49	0.36	0.73	0.52	0.63
#2	7.9	0.84	0.3	0.35	0.29	0.8
#1	4.26	0.69	0.63	0.91	0.54	0.55
#7	1.56	0.65	0.37	0.57	0.61	0.85
median	1.9	0.80	0.57	0.70	0.67	0.73

Figure S7: Schematic illustrating the ellipticity, sphericity, and roundness parameters used for quantifying the particle shape obtained from nano-CT reconstructed volumes.

In order to study with more details, the features observable within the NMC particles, regions of interest have been drawn in the 8-bit ring filtered images around seven different particles representative of the large variety found in the global population. The histograms of the grey values of the segmented particles have been represented along with the one corresponding to a subvolume of background (air) of nearly identical volume size in the closest area nearby. The peaks full width at half maximum are representative of the signal standard deviation respectively in the NMC particles and in the background. Then, the narrower shape of the background peak compared to the active material one's indicates that the wide dispersion of grey value in the particles are higher than the noise level in the background. In fact, the noise distributions of air volumes located nearby the studied particles in the final reconstructed volume after ring removal are only twice or three times sharper, meaning that the smallest features could be associated with noise in the reconstruction (see supplementary Fig.S8). This implies that this dispersion and the darker features in the images may be related to internal voids present in the NMC particles. The resulting void volume fraction and associated median size have been estimated from the images thanks to volume fraction and local thickness measurement. As between 10-35 % of voids cannot be reasonably identified within the spatial resolution limits ($\geq 50\,\mathrm{nm}$), it is not possible to quantify this void volume fraction with certainty but rather just give a rough minimum value of 10 % for the seven particles selected.
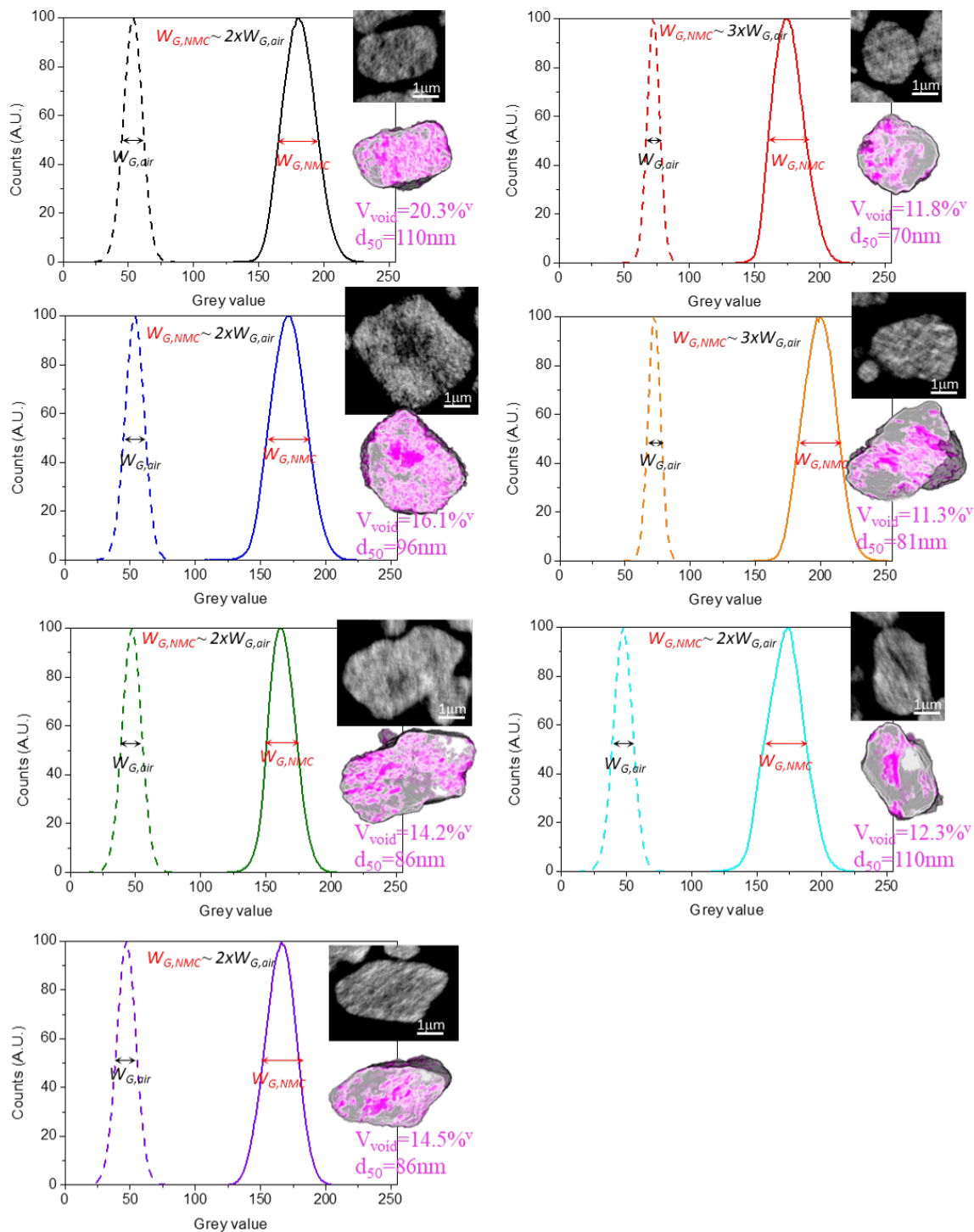
Figure S8: Normalized histograms of the NMC particle and air grey value (for identical volumes). The particle of interest are represented in the enclosed images (contrast fixed on the NMC particle peak) on the right corner along with a 3D representation of the particle with its internal void highlighted in magenta (with volume fraction and median size enclosed).

However, the signal over noise ratio (SNR) and contrast over noise ratio (CNR) are high for the acquired images, with respective estimated values of 8.8 and 2.3, entailing that most of the largest features inside of the particle should have a physical meaning. The estimation of the signal over noise ratio (SNR) has been performed on the raw projections of the scan, following the formula[4]:

$$SNR = \frac{mean(voxelofinterest)}{\sigma_{dev}(background)}$$

The contrast over noise ratio (CNR) have been estimated from the 32-bit floating images according to the formula:

$$CNR = \frac{mean(voxelofinterest) - mean(background)}{\sigma_{dev}(background)}$$

$$\text{with} \begin{cases} \text{mean (voxel of interest): } m_{NMC} = 5737 \\ \text{mean (background): } m_{air} = 4255 \\ \sigma_{dev}(background) : \sigma_{air} = 649 \end{cases}$$

Analyses of the void structure of the particles have been based on the 8-bit images ring filtered images. Peak analyses have been carried out using the peak analyser tool of the OriginPro© software from OriginLab Corporation.

Electrochemistry

The electrochemistry of the NMC was validated using previously published procedures.[S1] Briefly, 100 µm thick electrodes were prepared on Al foil using an ink composed of 95/5/5 wt% NMC/PVDF binder/ Super P conductive carbon dispersed in N-methyl-2-pyrrolidone, corresponding to an active material areal loading of $11\,\text{mg}\,\text{cm}^{-2}$. A coin cell was assembled using a 20 µm polyethylene separator, and Li foil. The electrolyte was 1M $LiPF_6$ in ethylene
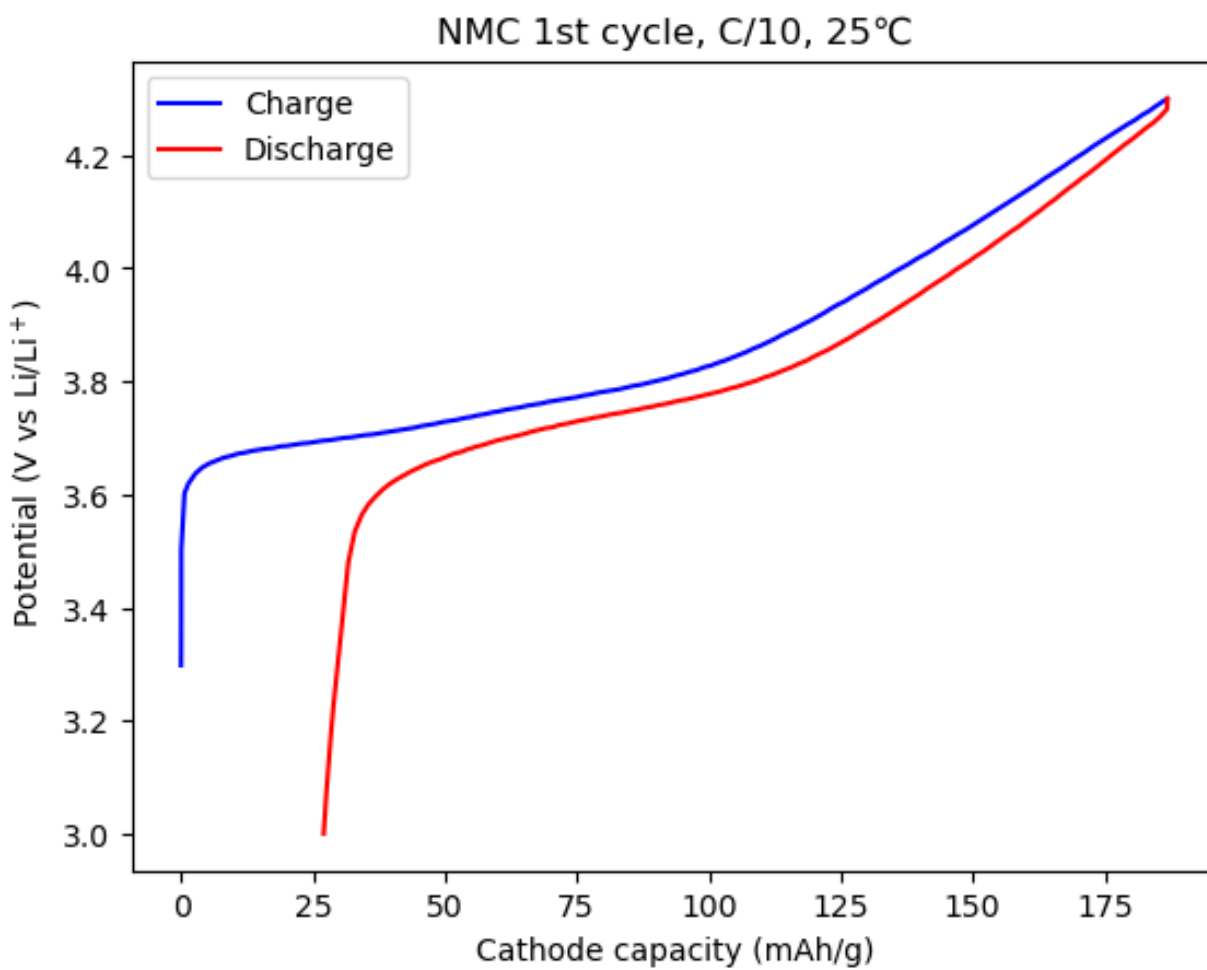
Figure S9: Electrochemistry of the NMC active material.

carbonate/dimethyl carbonate in 1/2 v/v ratio. The cell was cycled at C/10 to an upper potential limit of 4.3 V at 25 °C. The first cycle is plotted in Figure S9.

References

(S1) Paulsen, J.; Nelis, D.; Hu, J.; Zhu, L.; Robert, E. Precursors for cathode material with improved secondary battery performance and method to prepare the precursors. 2022.